Reduced Graphene Oxide Micromesh Electrodes for Large Area, Flexible, Organic Photovoltaic Devices

Dimitrios Konios, Constantinos Petridis, George Kakavelakis, Maria Sygletou, Kyriaki Savva, Emmanuel Stratakis, and Emmanuel Kymakis**

A laser-based patterning technique—compatible with flexible, temperature-sensitive substrates—for the production of large area reduced graphene oxide micromesh (rGOMM) electrodes is presented. The mesh patterning can be accurately controlled in order to significantly enhance the electrode transparency, with a subsequent slight increase in the sheet resistance, and therefore improve the tradeoff between transparency and conductivity of reduced graphene oxide (rGO) layers. In particular, rGO films with an initial transparency of ≈20% are patterned, resulting in rGOMMs films with a ≈59% transmittance and a sheet resistance of ≈565 Ω sq^{-1}, that is significantly lower than the resistance of ≈780 Ω sq^{-1}, exhibited by the pristine rGO films at the same transparency. As a proof-of-concept application, rGOMMs are used as the transparent electrodes in flexible organic photovoltaic (OPV) devices, achieving power conversion efficiency of 3.05%, the highest ever reported for flexible OPV devices incorporating solution-processed graphene-based electrodes. The controllable and highly reproducible laser-induced patterning of rGO hold enormous promise for both rigid and flexible large-scale organic electronic devices, eliminating the lag between graphene-based and indium–tin oxide electrodes, while providing conductivity and transparency tunability for next generation flexible electronics.

1. Introduction

Organic photovoltaics (OPVs) is a promising technology for future low cost energy supply due to its ability to employ flexible substrates enabling futuristic applications and mass production technologies such as roll-to-roll (r2r) manufacturing.[1–3] Being the first layer of an OPV device that comes in contact with the light, the transparent conductive electrode (TCE) is a vital determining factor to the device power conversion efficiency (PCE). Recently, OPV devices with efficiencies above 10% were certified, with their operation lifetimes exceeding industrially interesting levels.[4,5] Indium–tin oxide (ITO) is currently the dominant material used as TCE in rigid optoelectronic devices owing to its high transparency, T_r, in the visible spectrum and its good conductivity.[6] However, considering the employment of OPVs in everyday applications, the electrodes should be inexpensive, lightweight, and highly elastic in order to conserve their electrical properties under high stresses. In this context, ITO suffers from considerable limitations. First, it is expensive due to both the scarcity of indium reserves and the sputter deposition line expenses and second is not flexible, since its polycrystalline microstructure is brittle and cracks when the layer is bent or stretched repeatedly.[7] On top of that, indium is known to diffuse through the photoactive layer, leading to significant deterioration of the photovoltaic performance.[8–10] Therefore, the progress of flexible OPVs is much slower due to the lack of a flexible transparent and high conductive electrode; a r2r compatible substitutive material for ITO with a similar performance, but lower cost is highly desired.

Solution-processed carbon nanotubes,[11,12] metallic nanowires,[13] and conductive polymers[14] have been utilized as the TCE in organic electronic devices. However, they exhibit relatively high surface roughness or large sheet resistance, R_s, thus reducing the reproducibility rate of the devices.

Ever since the isolation of free standing graphene in 2004,[15] graphene research has experienced a phenomenal growth. Graphene can be produced by several techniques, including micromechanical exfoliation of graphite,[16] sonication-induced exfoliation,[17] thermal- or plasma-enhanced chemical vapor deposition (CVD) deposition from a carbon feedstock gas,[18] laser-induced exfoliation,[19] and carbon nanotubes unzipping by either laser[20] or chemical treatment.[21] Graphene's exceptional electronic, optical, and mechanical properties make it highly attractive, believed to be the next wonder material for optoelectronics and thus triggering the application of

D. Konios, Dr. C. Petridis, G. Kakavelakis, K. Savva
Dr. E. Stratakis, Prof. E. Kymakis
Center of Materials Technology and Photonics and
Electrical Engineering Department
Technological Educational Institute of Crete
Heraklion 71004, Crete, Greece
E-mail: stratak@iesl.forth.gr; kymakis@staff.teicrete.gr
Dr. C. Petridis
Department of Electronic Engineering
Technological Educational Institute of Crete
Chania 73132, Crete, Greece
M. Sygletou, K. Savva, Dr. E. Stratakis
Institute of Electronic Structure and Laser
Foundation for Research and Technology-Hellas
Heraklion 71110, Crete, Greece

DOI: 10.1002/adfm.201404046

© 2015 WILEY-VCH Verlag GmbH & Co. KGaA, Weinheim

graphene-based materials in the different layers of photovoltaic devices.[22–25] In particular, the enhanced electrical conductivity, combined with its high transparency in visible and near-infrared spectra,[26] emerged graphene as an ideal low cost ITO substitute.

CVD has been reported as the most successful approach to produce highly transparent and low R_s graphene electrodes.[27] Nonetheless, the grown graphene films have to be transferred onto a target substrate through a complicated process, increasing the manufacturing cost. An alternative low cost approach compatible with r2r mass production is the chemical exfoliation of graphene oxide (GO) either by ultrasonic dispersion or rapid thermal expansion followed by reduction with proper chemical[28] or laser-assisted routes.[29] The reduced GO (rGO) can be easily produced in bulk quantities as graphene ink,[30] taking advantage of its improved soluble character in common solvents.[31] In this context, there was an extensive research effort on the utilization of rGO as the TCE in OPVs.[32–34] Nonetheless, the recorded PCEs remain low (≈1.0%), mainly due to the low T_r (70%) and high R_s of the rGO films (≈1 kΩ sq^{-1}), compared to the highly commercialized ITO (90%, 15 Ω sq^{-1}). In the same context, our group has recently demonstrated an efficient laser-based reduction method for fabricating flexible conductive and transparent graphene films that can be spin-casted on temperature-sensitive substrates. The femtosecond (fs) laser-treated rGO (LrGO) films with 70% T_r and R_s of 1.6 kΩ sq^{-1} were integrated in polymer–fullerene photovoltaic cells, as the TCE leading to an efficiency of 1.1%.[35] Therefore, it is evident that pristine rGO films cannot compete with ITO, due to their extremely high R_s (>1 kΩ sq^{-1}) for high transparency values.

One of the most eye-catching strategies for increasing the transparency of a TCE material is the employment of a mesh structure with periodic lines, as applied in copper[36] and silver[37] network mats. Their R_s and transparency can be controlled by varying the grid width, spacing, and thickness.[38] In this way, the transparency of the mesh film can be significantly increased compared with the pristine film, while the R_s alternation is minimal; the percolated network can conduct current even with the presence of large empty spaces. In this context, various patterning techniques were developed, such as lithography with block copolymer,[39] ion beam,[40] plasma etching,[41,42] template method,[43] and chemical etching.[44] Most recently, rGO meshes fabricated using standard photolithography and O_2 plasma methods were utilized as the TCE in OPVs,[45,46] while laser-induced patterning of GO[47] has been reported for energy storage[48] and memory applications.[49] However in both cases, the employment of a mask aligner and the additional process step of the photoresist removal by O_2 plasma, induce high cost and complexity in the device fabrication.

In contrast to photolithography patterning, fs laser patterning[50] has been proposed as a versatile tool for high precision patterning on a wide range of materials[51] and in large scale.[52] The main advantage of the induced fs laser patterning is that it can be applied to temperature-sensitive substrates, such as polyethylene terephthalate (PET), without practically affecting its integrity during processing. In this work, we propose a low cost, high throughput, fully scalable, and facile technique for one-step patterning of rGO films on PET or glass substrates based on fs laser irradiation. This technique which can be easily controlled over the entire illuminated area induces minimum thermal damage in the surrounding layers and more importantly is compatible to r2r production processes.[53] Furthermore, direct laser patterning has the advantage of arbitrary designability and reasonably high spatial resolution.[54] By utilizing this methodology, rGO micromeshes (rGOMM) are fabricated, enabling to overcome the tradeoff between R_s and T_r of pristine rGO layers. The optoelectrical properties of rGO thin films are found to be directly dependent on the interplay between the periodicity and the geometrical characteristics of the mesh pattern structure. Approximately 100 nm thick rGO films with 22.5% T_r can be patterned to form TCEs with significantly increased T_r (up to ≈85%), and simultaneous tuning of the film conductivity and sheet resistance. As a proof of concept, we successfully employed the rGOMM as the TCE in small and large active area of (poly[*N*-9′-heptadecanyl-2,7-carbazole-alt-5,5-(4′,7′-di-2-thienyl-2′,1′,3′ benzothiadiazole)]) (PCDTBT):[6,6]-phenyl C_{71} butyric acid methyl ester ($PC_{71}BM$) based air processed OPV device, achieving PCE values of 3.67% and 3.05% on glass and flexible substrates, respectively. To the best of our knowledge, these are the highest PCEs reported for a solution-processed graphene-based TCE in OPVs. This laser-based patterning technique can be considered as a universal strategy in order to fabricate large-scale graphene films with controlled electrical and optical properties for various flexible electronic device components.

2. Results and Discussion

The as-prepared, using the modified Hummers' method,[55] GO was dispersed in water to form stable aqueous solutions. Vacuum filtration technique was used to deposit uniform layers of GO on top of mixed cellulose ester (MCE) membrane. The thickness and the homogeneity of the GO films can be accurately controlled by simply varying either the concentration of the GO solution or the filtration volume. The prepared GO films were transferred on glass and PET substrates for further treatment. To restore the conjugated structure of graphene and improve the films conductivity, chemical reduction is performed by exposing the GO films to hydriodic acid/acetic acid (HI/AcOH).[56] Figure S1 (Supporting Information) presents the x-ray photoelectron spectroscopy (XPS) survey spectra of GO and rGO, indicating that most oxygen-containing groups are effectively removed during HI/AcOH reduction.

Nitric acid (HNO_3) has been widely used as p-type dopant to improve the conductivity and charge transfer efficiency of carbon structures.[27,57] Figure S2a (Supporting Information) presents the correlation of R_s and T_r at 550 nm of rGO films to their thicknesses. Both T_r and R_s decrease with increasing film thickness, highlighting the inherent tradeoff between the two factors. The R_s as a function of transmittance before and after HNO_3 treatment is demonstrated in Figure S2b (Supporting Information). It is clear that R_s shifts to lower values (≈27% decrease) after additional treatment by dipping the prepared rGO films in a HNO_3 bath (65%) for 1 h.

© 2015 WILEY-VCH Verlag GmbH & Co. KGaA, Weinheim

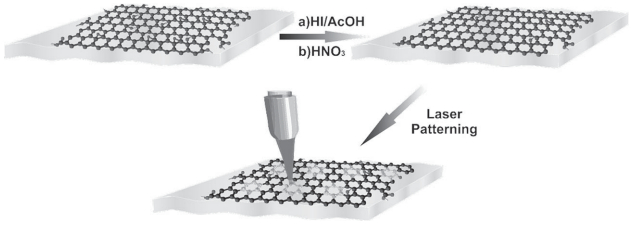

Figure 1. Schematic illustration of the rGO mesh electrodes preparation.

The selective laser patterning of rGO on top of glass or PET (**Figure 1**a) was performed with the delivery of UV ultrashort laser pulses (248 nm, 500 fs) with 1 Hz repetition rate. Unlike previous studies,[58] the proposed process is one-step and does not require time-consuming and labor-intensive lithography; no complex masks, postprocessing, or clean room facilities are required. Even though it is a point-by-point patterning technique, the processing rate can be significantly increased using high repetition laser sources and multiple beam interference irradiation schemes.[59] Besides this, it is a fully automated technique, allowing processing of the rGO layers according to preprogrammed patterns. In our experiments, the rGO mesh periodicity, the number of pulses per pit, as well as the neck width of the mesh could be readily controlled.

The physical processes (Figure S3, Supporting Information) that follow fs laser–matter interactions are various and occur in different timescales. Specifically, the laser pulse energy is initially absorbed by the electrons and is transferred to the lattice over a picosecond timescale. Within a few nanoseconds a shock wave is propagating away from the electron plasma. On the microsecond timescale, the thermal energy diffuses out of the focal volume. The heat generation can be finely controlled by several factors including layer absorption properties, laser power, number of pulses per spot, and beam profile. For a certain beam and above a minimum laser energy value, single-shot ablation can be observed that causes permanent structural changes. In our case, the excimer laser beam used had a rectangular intensity profile and its energy per pulse was adjusted with the aid of a half-wave plate. Besides this, the focusing optics defined the focal volume and thus the mesh pattern size (the latter is also defined by the number of laser pulses)[60] and its symmetry.[61] It was observed that the minimum laser fluence required to partially remove rGO was 386 mJ cm^{-2}; this fluence was enough to attain a strong optical contrast between the processed and nonprocessed area, observed by optical microscopy. Upon increasing the laser pulse energy or the number of pulses per irradiating spot (exposure time), the irradiance is increased and consequently the ablated depth.

It is found that the ablation or pit depth is a key factor that determines the transparency and sheet resistance of laser-patterned rGO layers. Besides this, the number of fs laser pulses needed to achieve the optimum tradeoff between T_r and R_s is determined by the rGO layer thickness (initial T_r) and the substrate over which the film has been deposited. As we have previously demonstrated, the primary advantage of utilizing fs laser irradiation lies in the ability of in situ controlled epidermal treatment giving rise to minimum induced thermal effect on the supporting substrate.[35] This, in turn, enables for selective removal of the rGO material without practically affecting the integrity, even of thermally sensitive substrates underneath. It further allows the progressive removal of rGO upon using a series of pulses. This is in contrast to our experimental observation that the use of longer pulse duration gives rise to, uncontrolled, explosive ablation of the thin layer, causing the merge of neighboring mesh features, as well as thermal distortion of flexible substrate due to heat of the accumulation effects. Both effects were found to be detrimental to the conductivity of the treated rGO layers.

The effectiveness of laser patterning has been examined on the frame of the composition and surface morphology differences between the pristine and irradiated areas. The former were investigated through Raman spectroscopy, whereas the latter were examined by atomic force microscopy (AFM). The progressive material removal induced upon increasing the number of irradiation pulses, N, is demonstrated by the Raman spectra of the pristine and laser-patterned regions of the rGO mesh on glass, using $N = 2$ and $N = 3$ laser pulses of the threshold fluence, respectively (Figure S4, Supporting Information). The appearance of the D (1359 cm^{-1}) and G (1578 cm^{-1}) peaks in the irradiated area for $N = 2$ but with decreased intensity, demonstrates the partial etching of rGO from the irradiated areas. At the same time, a Raman peak at 1045 cm^{-1} corresponding to the glass substrate becomes more pronounced. On the contrary, for $N = 3$ the rGO peaks disappear, indicating the complete removal of the rGO layer. AFM was employed to observe the difference in the surface morphology of irradiated and nonirradiated areas on the rGO films. Figure S5 (Supporting Information) demonstrates a quite homogeneous and smooth surface for the nonirradiated area, with a root-mean-square (rms) roughness value of 1.59 nm. Following laser treatment with $N = 2$, the rms roughness was increased to 6.99 nm due to the abrupt ablation process.

Figure 2b presents scanning electron microscopy (SEM) images of the laser-generated rGO mesh patterns obtained upon irradiation with $N = 2$ at the threshold fluence. The bright spots in the illumination area reveal the partial ablation of the rGO layer, which is in agreement with the respective Raman spectra. In addition, the observed mesh pattern spatially shape variations are mainly due to small laser pulse energy fluctuations. Regarding the optimum neck width of the mesh, it should be as small as possible in order to reduce the losses due to light shadowing effects on the one hand and to retain the sheet conductivity on the other.

One of the key challenges in rGO microelectronic devices applications is to tune the relation of T_r and R_s in a controllable

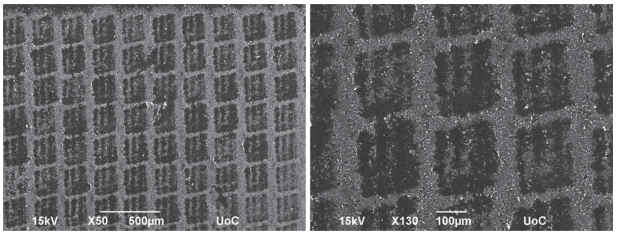

Figure 2. SEM images of the laser-induced mesh patterns. The samples have been irradiated with $N = 2$ fs pulses of 386 mJ cm^{-2} fluence. The laser-generated mesh has a period of 250 µm and the transparency has increased by ≈48%.

© 2015 WILEY-VCH Verlag GmbH & Co. KGaA, Weinheim

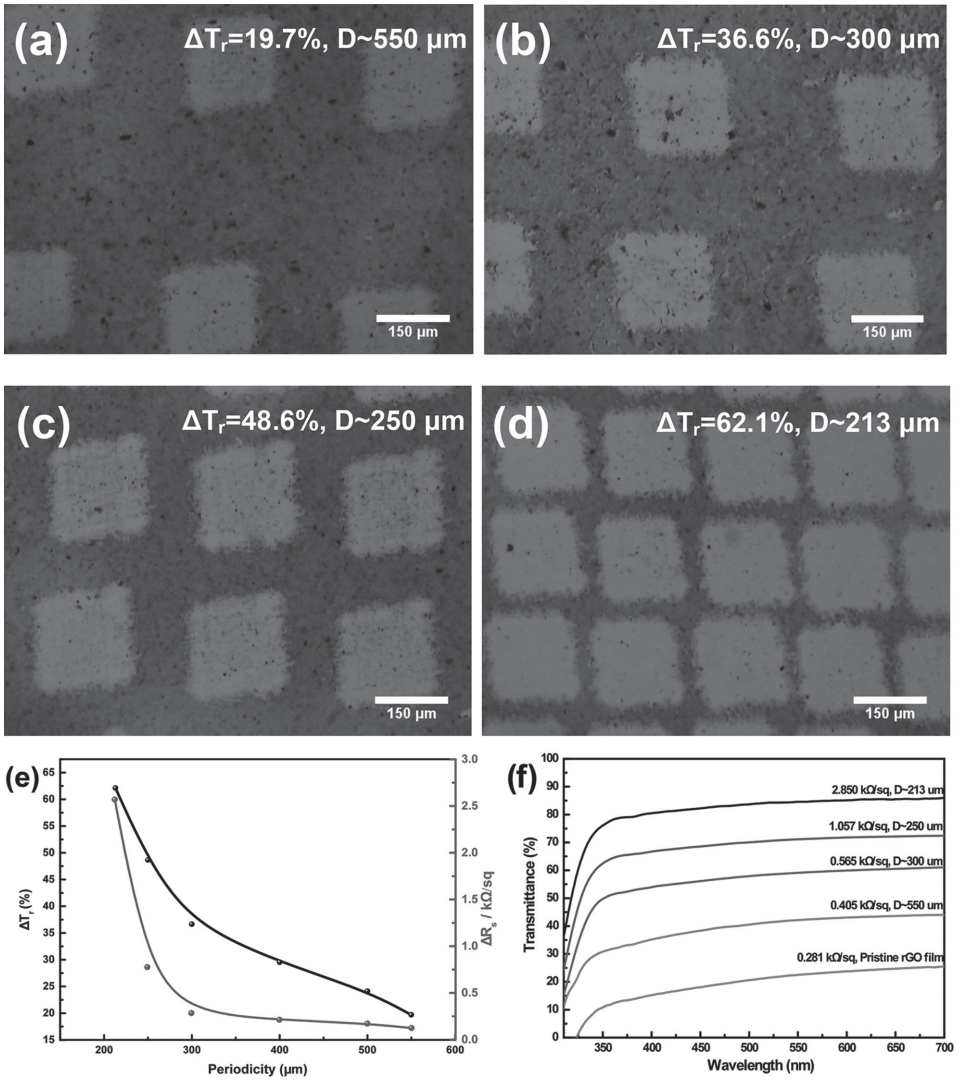

Figure 3. Optical microscopy images of laser-generated rGOMMs demonstrating the effect of the mesh periodicity on the film transmittance. Transparency was increased by a) ΔT_r = 19.7%, b) ΔT_r = 36.6%, c) ΔT_r = 48.6%, d) ΔT_r = 62.1% with ≈550, ≈300, ≈250, and ≈213 μm periodicity, respectively. e) Transmittance difference at 550 nm (ΔT_r) and sheet resistance difference (ΔR_s) as a function of the periodicity (D) of the laser-induced rGOMM. The starting values for the pristine rGO layer were T_r = 22.5% and $R_s \approx 281\ \Omega\ sq^{-1}$. f) Optical transmittance spectra of rGOMMs with different periodicities, also demonstrating the R_s values of the rGO film after the laser patterning.

manner.[62] The attractiveness of the technique proposed here is that it permits such fine tuning via variation of the irradiation dose (energy, number of pulses) and/or the periodicity and thus the neck width of the mesh. For instance, **Figure 3**a–d demonstrate the progressive increase of T_r upon variation of the periodicity, D, of the rGOMMs pattern using the threshold fluence. Although the initial T_r of the rGO layer was ≈20% it was significantly improved to ≈85% for D≈213 μm (**Figure 4**d). At the same time, as shown in Figure 3e, the layer conductance slightly decreases, which is highly desirable for TCE applications. It should be noted here that, regardless of the substrate used, the lowest conductance changes can be only achieved provided that a continuous rGO film is realized after the laser patterning process, i.e., without complete removal of GO at the irradiated areas.

The cost effectiveness of the presented laser patterning technique can be supported by the following: (a) it does not require any strict operational conditions or complex facilities, compared to other techniques like e-beam and ion beam lithography,[63] (b) it provides high flexibility for arbitrary graphene oxide patterning since it is noncontact and computer driven, (c) it is maskless in contrast to other patterning techniques,[64] (d) the use of fs laser pulses make it compatible with flexible, low cost substrates, (e) it is a one-step and not time-consuming process, (f) it is operated under open air and room temperature conditions, and (g) the fabrication setup is simple and easily controllable. Finally, the laser-assisted maskless patterning is easily reproducible since its key parameters, laser irradiance and micromesh periodicity, can be controlled with high precision.

Compared with previously established patterning techniques, the presented laser-based method exhibits unique advantages. It is a one-step method, since no grid-like patterning masks,[65] or any further transfer steps, are required. In addition, there

© 2015 WILEY-VCH Verlag GmbH & Co. KGaA, Weinheim

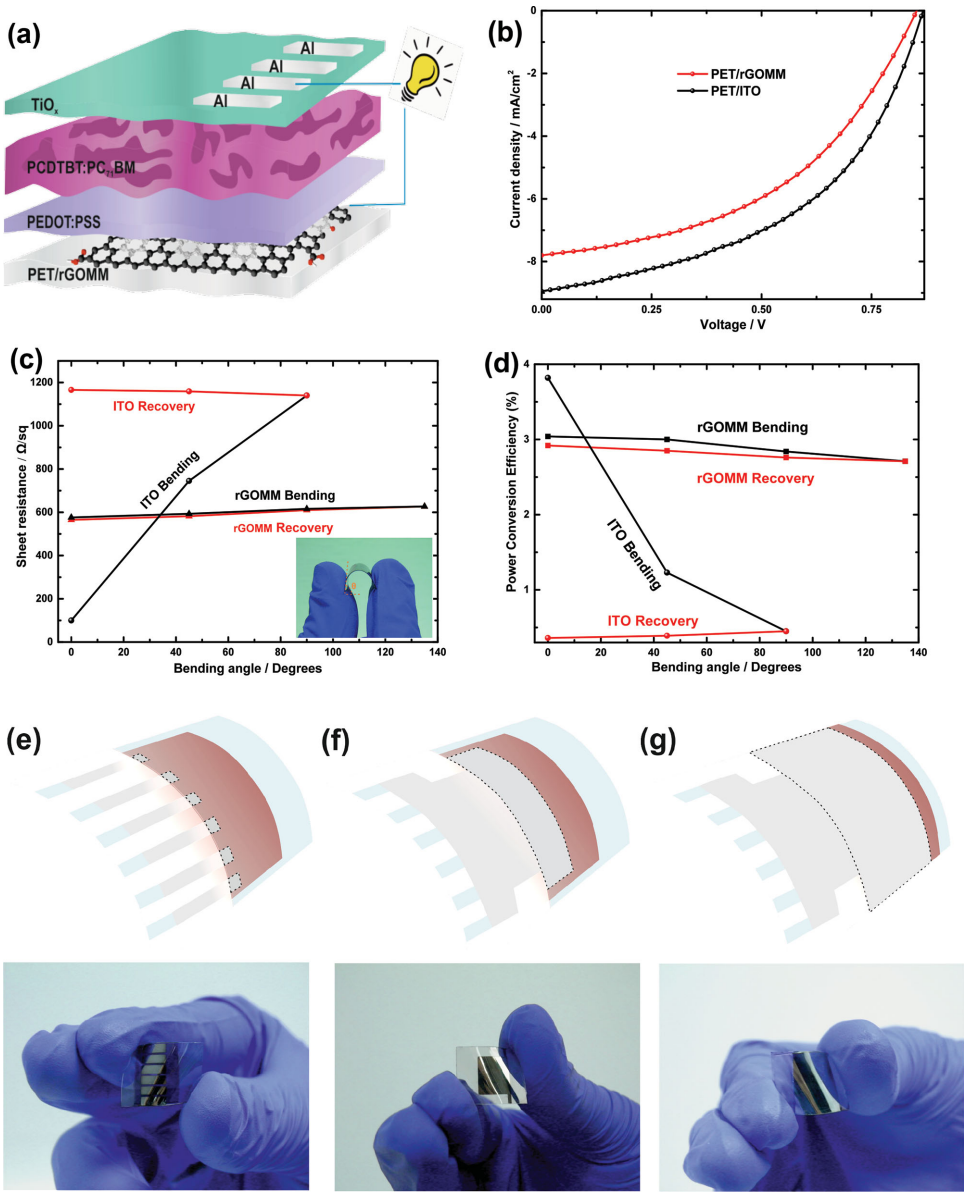

Figure 4. a) Schematic illustration of BHJ OPV device with the laser-induced rGOMM as TCE. b) The illuminated current–voltage (*J*–*V*) curves of the solar cells with rGOMM (red) and ITO (black) as TCE. c) Sheet resistance versus device bending angle of rGOMM- and ITO-based OPV cells. The inset photo represents a rGOMM-based device subjected to bending. d) Power conversion efficiency of rGOMM- and ITO-based flexible devices under and after bending at certain angles. Schematic illustration and photographs of devices exhibiting increased active areas; e) 4, f) 50, and g) 135 mm^2.

is no need of any photoresistive material[66] or prepatterned elastomeric stamps,[67] while the use of fs laser pulses allows the pattering of microsize holes on top of flexible, temperature-sensitive, and low cost materials. Finally, its operation can be performed under ambient and it is fully automated, since all the patterning parameters—mesh period and laser parameters—are precisely controlled by a specially designed software. The main disadvantage of the proposed laser technique is related with the finer mesh dimensions attainable, which are optical diffraction-limited. As a result, the technique can provide micrometer- or at most submicrometer-sized patterns, contrary to nanosized features that can be achieved by other competitive methods.[39]

As a proof of the potential application of the proposed method for the fabrication of high performance transparent electrodes, we applied the rGOMM layers as the bottom TCE layer in flexible OPV devices, aiming to identify the optimum combination of T_r and R_s leading to the best PCE. For this purpose, we have used the rGOMM meshes demonstrated in Figure 3e,f. Devices were fabricated on PET substrates and the performance of OPV devices with PCDTBT:$PC_{71}BM$ photoactive blends deposited on rGOMMs was compared with those deposited on ITO. The OPV devices structure employed is schematically presented in Figure 4a, with holes collected in the TCE electrode and electrons in the Al metal electrode. Figure 4b presents the illuminated *J*–*V* characteristics for the best performed OPV device

© 2015 WILEY-VCH Verlag GmbH & Co. KGaA, Weinheim

Table 1. Averaged photovoltaic parameters of the solar cells incorporating rGO, rGOMMs, and ITO as TCE (standard deviations in Figure S6b, Supporting Information).[a)]

PET/rGOMM (T, R_s)	J_{sc} [mA cm^{-2}]	V_{oc} [mV]	FF [%]	PCE [%]
22.5%, 281 Ω sq^{-1} (pristine rGO film)	4.51	837	47.2	1.78
42.2%, 405 Ω sq^{-1}	6.52	843	46.4	2.55
59.1%, 565 Ω sq^{-1}	7.81	848	45.9	3.05
71.1%, 1057 Ω sq^{-1}	3.72	840	42.3	1.32
84.6%, 2850 Ω sq^{-1}	2.37	832	37.6	0.74
PET/ITO	8.93	864	49.5	3.82

[a)]Average photovoltaic characteristics for OPV devices with different TCEs. To account for experimental errors, the reported averages for each case are taken for ten identical devices, consisting of six cells each.

incorporating rGOMM as TCE, compared with the control ITO-based one, while **Table 1** summarizes the averaged photovoltaic parameters of the whole series of OPV devices measured. The standard deviations of all measured quantities are presented in Figure S6b (Supporting Information).

It can be clearly observed that the open circuit voltage (V_{oc}) remains almost constant for all devices, which is reasonable, considering that its value is derived by the energy levels offset between the highest occupied molecular orbital (HOMO) of PCDTBT and lowest unoccupied molecular orbital (LUMO) of $PC_{71}BM$. On the other hand, a tradeoff between the photocurrent (J_{sc}) and fill factor (FF) is observed. In particular, the J_{sc} is increased as the T_r of the rGOMM layer becomes higher, up to the limit that R_s remains in the same order of magnitude compared to the starting material. The FF is mainly affected from the R_s of TCE, thus is constantly decreased as the mesh structure becomes denser. As can also be seen by the 3D graph of Figure S7 (Supporting Information), the optimum photovoltaic parameters for the rGOMM-based devices were extracted for $T_r \approx 59.1\%$ and $R_s \approx 565\ \Omega\ sq^{-1}$, with a resulting PCE of 3.05%.

Furthermore, OPV devices incorporating rGO films with different thicknesses and therefore different T and R_s pairs were also fabricated and characterized (Table S1, Supporting Information). In this way, a direct comparison of the PV performance of the optimum devices, utilizing unpatterned rGO and patterned rGOMM films, can take place. It can be clearly seen that the performance of the rGOMM-based devices is superior to the devices, which utilize rGO films, mainly due to the difference in R_s, which has a strong effect on the devices FF. In particular, the unpatterned rGO-based device exhibits a maximum PCE of 2.12%, while the rGOMM-based device exhibits a PCE of 3.05%. Also, the device which utilizes rGO as the TCE with approximately the same transparency as the rGOMM film (60.3% and 59.1%, respectively) exhibits an even lower PCE of 2.12%, due to the significant difference in the R_s of the TCE. Therefore, the laser patterning technique clearly enables us to improve the tradeoff between T_r and R_s of the rGO films, since patterned films with the same transparency as the unpatterned rGO films exhibit much higher conductivity values.

Another important benefit of the flexible rGOMM electrode on PET substrate is its high durability under extreme bending conditions and its ability to retain its electrical properties. This capability is very important for every flexible electronic device. Indeed, as shown in Figure 4c the R_s change upon 90° bending is negligible, as it does not change more than 8%, while the overall change is ≈11% up to a bending angle of 135°. Following the reverse route, the R_s returns near to its initial value, showing a slight increase (less than 2%). This implies that no appreciable change in the TCE structure occurs during bending. This excellent flexibility is advantageous over the conventional ITO, which showed a rapid increase in its R_s value under identical bending conditions (also shown in Figure 4c). This behavior can be attributed to the well-reported cracking effect of ITO that gives rise to a catastrophic electrical failure.[68]

An important motivation for using solution-processed rGOMM electrodes is to realize highly flexible OPVs that can be used for compact roll-type solar modules. A similar behavior with above findings is observed in Figure 4d where the photovoltaic performance with respect to the device bending history is presented. Indeed, the rGOMM-based device almost retains its initial photovoltaic performance after extreme bending conditions, a result that is highly desired for flexible organic electronic applications. On the contrary, ITO-based devices showed a remarkable different behavior; the device could operate only up to 45° bending, but with a significant deterioration in its performance, while it is completely destroyed after 90° bending, without the ability of retaining its initial PCE values.

Another important issue investigated in this work was whether our proposed method can be applicable to large area OPV devices (Figure 4e–g). This is crucial for the future development of this technology and its subsequent upscaling from single cells to solar modules. For this purpose, rGOMM- and ITO-based devices with increasing active area were fabricated and tested. As it can be clearly observed in **Table 2**, the deterioration in the photovoltaic performance measured for both rGOMM- and ITO-based devices was practically the same, i.e., for 135 mm^2 active area PCE reduction measured was 63.2% for ITO and 64.9% for rGOMM, respectively. It can be concluded that the proposed electrode patterning method can be effectively applied to large area photovoltaic cells without compromising the photovoltaic efficiency.

The contribution of our work in the graphene-based TCE technology reported to date is illustrated in **Figure 5**. The figure indicates the PCE values of OPV devices fabricated on

Table 2. Summary of the averaged photovoltaic parameters for optimum rGOMM and ITO electrodes with different device active area.

	Device area [mm^2]	J_{sc} [mA cm^{-2}]	V_{oc} [mV]	FF [%]	PCE [%]
rGOMM	4	7.81	848	45.9	3.05
	50	5.44	846	38.9	1.79 (41.1%↓)
	135	3.87	831	33.2	1.07 (64.9%↓)
ITO	4	8.93	864	49.5	3.82
	50	6.31	862	42.5	2.31 (39.5%↓)
	135	4.48	848	36.3	1.38 (63.2%↓)

© 2015 WILEY-VCH Verlag GmbH & Co. KGaA, Weinheim

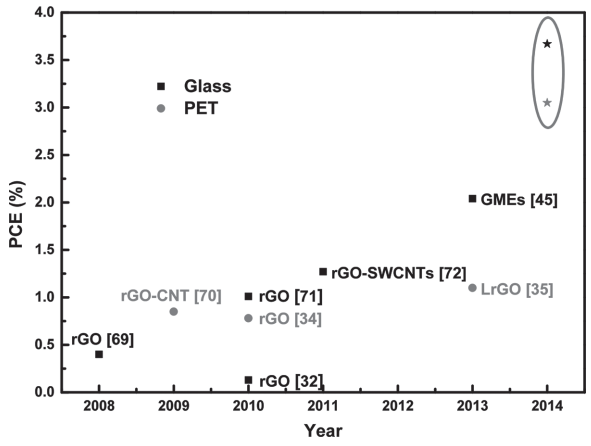

Figure 5. OPVs performance of OPV cells based on solution-processed graphene-based TCEs reported to date in the literature.[32,34,35,45,69–72] Black squares stand for rigid devices, while red circles for devices on flexible substrates. Stars illustrate the contribution of this work to the PCE improvement.

solution-processed graphene-based TCE reported in the literature, together with the corresponding values of rGOMM-based devices reported here. Devices on rigid as well as flexible substrates are taken into account. It is more than clear that the proposed laser patterning technique produces high-quality rGOMM electrodes and could potentially mitigate the lag between graphene-based and ITO-based TCEs (Table S2, Supporting Information).

3. Conclusion

In conclusion, the successful development of a direct fs laser writing technique to fabricated pattern rGO mesh TCEs has been demonstrated. The technique enables the accurate control of rGO micromesh geometrical features on top of rigid (glass), as well as flexible (PET) substrate. As a result, the conductivity and transparency of the treated rGO films can be finely tuned and tailored for the specific application. Using this technique, it is shown that rGO electrode transparency can be readily changed from ≈20% to up to ≈85%, with only a slight increase in the respective R_s value. To demonstrate the application and the potential applicability of the proposed technique in the field of flexible transparent electronics, OPV devices that host the laser-induced rGOMMs films as the TCE electrode were fabricated, exhibiting superior performance compared to the ones that incorporate pristine rGO TCEs. The devices displayed a PCE of 3.05%, which is the highest reported to date for flexible OPV devices incorporating solution-processed graphene-based electrodes. Due to their chemical stability, mechanical flexibility, high transparency, and conductivity, along with their scalable production through solution processing and subsequent laser patterning, rGOMMS are excellent potential candidates for a wide range of new applications with tunable optoelectrical properties, including flexible electronic OPVs, perovskite solar cells, organic light emitting diodes, and photosensors, as well as traditional electronic devices based on rigid substrates.

4. Experimental Section

Preparation of GO:[55] GO was prepared from graphite powder (Alfa Aesar, ≈200 mesh) according to a modified Hummers' method. In more detail, graphite powder (0.5 g) was placed into a mixture of H_2SO_4 (40 mL, 98%) and $NaNO_3$ (0.375 g). The mixture was then stirred and cooled in an ice bath. While maintaining vigorous stirring, $KMnO_4$ (3.0 g) was then added in portions over a period of 2 h. The reaction mixture was left for 4 h in order to reach room temperature before being heated to 35 °C for 30 min. It was then poured into a flask containing deionized water (50 mL) and further heated to 70 °C for 15 min. The mixture was then decanted into deionized water (250 mL) and the unreacted $KMnO_4$ was removed by adding 3% H_2O_2. The reaction mixture was then allowed to settle and decanted. The graphite oxide obtained was then purified by repeated centrifugation and redispersed in deionized water until neutralized pH was achieved. Finally, the resulting GO was dried at 60 °C in a vacuum oven for 48 h before use.

Preparation of rGO Films: GO films were prepared by vacuum filtering the aqueous solutions of GO through mixed cellulose ester membranes (0.025 μm, Millipore). By either varying the filtration volume or the concentration of GO in the solution, films with varied thicknesses and thus different transparencies can be produced. In this case, the initial concentration of the GO solution used for film preparation was 5 mg L^{-1}. Aliquots of the GO solution were further diluted in water, sonicated to achieve exfoliated sheets of GO, and filtrated. The GO-coated membrane was cut into the desired sizes, immersed in deionized water to be wetted, and placed with the film side down onto the substrate (PET and glass) surface. The GO film was allowed to dry and adhere to the substrate at room temperature under a 1 kg weight. After 5 h the membrane was removed, leaving the GO films on the substrates, which were dried in a 60 °C oven. The process is highly repeatable and the films are well adhered to glass and plastic substrates. The reduction of GO films can be performed by exposing them to hydriodic acid (55%)/acetic acid vapor.[56] In detail, the as-prepared PET/GO and glass/GO films were placed on a stand inside a small desiccator that contained a mixture of HI (2.0 mL) and AcOH (5.0 mL). The desiccator was sealed and placed in an oil bath at 40 °C for 24 h. The films were then washed with methanol and dried at 60 °C in an oven. For the R_s improvement, the prepared rGO films were subjected to additional chemical treatment, by dipping them in a HNO_3 bath for 1 h, followed by cleaning and drying the surface under nitrogen steam.[27,57]

Fabrication of rGO Nanomesh: The rGO films were mounted on a computer controlled motorized *X*–*Y* translation stage. During the irradiation, the rGO films were scanned in two orthogonal directions (*X* and *Y*) in a fully controlled manner across a focused excimer laser beam (fluence ≈ 0.4 J cm^{-2}, beam size 0.02 mm^2, pulse width 0.5 ps, repetition rate 1 Hz, emission wavelength 248 nm). The dependence of the transparency of the rGO films with the mesh periodicity was examined by controlling the movement step of *X*–*Y* stage. As a result of laser irradiation, part of the irradiated material was ablated in order to achieve higher transparency. By increasing the number of laser pulses, greater amount of the irradiated material was removed.

Device Fabrication and Measurements: PCDTBT and $PC_{71}BM$ were purchased from Solaris Chem. PCDTBT:$PC_{71}BM$ were dissolved in 1,2-dichlorobenzene: Chlorobenzene (3:1) (*o*-DCB:CB) in a 1:4 (4:16 mg) ratio and stirred for at least 72 h at 80 °C before used. The ITO-based photovoltaic devices were fabricated on 20 × 15 mm ITO-coated PET substrates with R_s of 100 Ω sq^{-1} (Sigma-Aldrich). The rGOMM electrodes were prepared on flexible PET (Goodfellow) substrates (20 × 15 mm) with 90 μm thickness. The impurities were removed from the substrates through a three-step ultrasonication cleaning process (deionized water with soap, aceton, IPA). As a buffer layer, poly(ethylene-dioxythiophene) doped with poly(4-styrenesulfonate) (PEDOT:PSS), purchased from Heraeus, was spin-cast from an aqueous solution on the rGOMM and ITO-coated electrodes with a layer thickness of the layer was 20 and 30 nm, respectively, followed by baking for 15 min at 120 °C inside a nitrogen-filled glove box. The PCDTBT:$PC_{71}BM$ photoactive layer was subsequently deposited by spin-coating the blend solution at 1000 rpm

© 2015 WILEY-VCH Verlag GmbH & Co. KGaA, Weinheim

on top of PEDOT:PSS layer until the thickness reaches approximately 70 nm, followed by drying at 60 °C for about 5 min under inert condition. Titanium suboxide (TiO_x), used as the electron transport layer, was prepared according to a literature method.[73] TiO_x was dissolved in methanol (1:200) and then spin-coated to a thickness of approximately 10 nm (6000 rpm, 40 s) in air.[74] The samples were heated at 80 °C for 1 min in air. Finally, 100 nm of Al was deposited through a shadow mask by thermal evaporation on the devices. The whole device fabrication occurred in ambient conditions. The performances of the devices were measured at room temperature with an Air Mass 1.5 Global (A.M. 1.5 G) solar simulator at an intensity of 100 mW cm^{-2}. A reference monocrystalline silicon solar cell from Newport was used to calibrate the light intensity. All measurements were carried out in air immediately after device fabrication without encapsulation process.

Supporting Information

Supporting Information is available from the Wiley Online Library or from the author.

Acknowledgements

D.K. and C.P. contributed equally to this work. The research leading to these results has received funding from the European Union Seventh Framework Programme under Grant Agreement No. 604391 Graphene Flagship.

Received: November 15, 2014
Revised: December 8, 2014
Published online: January 28, 2015

[1] N. S. Sariciftci, L. Smilowitz, A. J. Heeger, F. Wudl, *Science* **1992**, *258*, 1474.
[2] G. Yu, J. Ga, J. C. Hummelen, F. Wudl, A. J. Heeger, *Science* **1995**, *270*, 1789.
[3] G. Li, R. Zhu, Y. Yang, *Nat. Photon.* **2012**, *6*, 153.
[4] M. A. Green, K. Emery, Y. Hishikawa, W. Warta, E. D. Dunlop, *Prog. Photovolt.: Res. Appl.* **2014**, *22*, 701.
[5] M. C. Scharber, N. S. Sariciftci, *Prog. Polym. Sci.* **2013**, *38*, 1929.
[6] S. H. Park, A. Roy, S. Beaupre, S. Cho, N. Coates, J. S. Moon, D. Moses, M. Leclerc, K. Lee, A. J. Heeger, *Nat. Photon.* **2010**, *3*, 297.
[7] D. S. Hecht, L. Hu, G. Irvin, *Adv. Mater.* **2011**, *23*, 1482.
[8] a) J. B. Wu, M. Agrawal, H. A. Becerril, Z. N. Bao, Z. F. Liu, Y. S. Chen, P. Peumans, *ACS Nano* **2010**, *4*, 43; b) W. J. da Silva, H. P. Kim, A. R. B. M. Yusoff, J. Jang, *Nanoscale* **2013**, *5*, 9324.
[9] B. Paci, G. Kakavelakis, A. Generosi, G. Wright, C. Ferrero, D. Konios, E. Stratakis, E. Kymakis, unpublished.
[10] B. Paci, D. Bailo, V. Albertini, J. Wright, C. Ferrero, G. D. Spyropoulos, E. Stratakis, E. Kymakis, *Adv. Mater.* **2013**, *25*, 4760.
[11] T. P. Tyler, R. E. Brock, H. J. Karmel, T. J. Marks, M. C. Hersam, *Adv. Energy Mater.* **2011**, *1*, 785.
[12] E. Kymakis, E. Stratakis, E. Koudoumas, C. Fotakis, *IEEE Trans. Electron Devices* **2011**, *58*, 860.
[13] S. De, T. M. Higgins, P. E. Lyons, E. M. Doherty, P. N. Nirmalraj, W. J. Blau, J. J. Boland, J. N. Coleman, *ACS Nano* **2009**, *3*, 1767.
[14] S. I. Na, S. S. Kim, J. Jo, D. Y. Kim, *Adv. Mater.* **2008**, *20*, 4061.
[15] K. S. Novoselov, A. K. Geim, S. V. Morozov, D. Jiang, Y. Zhang, S. V. Dubonos, I. V. Grigorieva, A. A. Firsov, *Science* **2004**, *306*, 666.
[16] K. S. Novoselov, D. Jiang, F. Schedin, T. J. Booth, V. V. Khotkevich, S. V. Morozov, A. K. Geim, *Proc. Natl. Acad. Sci. U.S.A.* **2005**, *102*, 10451.
[17] Y. Hernandez, V. Nicolosi, M. Lotya, F. M. Blighe, Z. Sun, S. De, I. T. McGovern, B. Holland, M. Byrne, Y. K. Gun'Ko, J. J. Boland, P. Niraj, G. Duesberg, S. Krishnamurthy, R. Goodhue, J. Hutchison, V. Scardaci, A. C. Ferrari, J. N. Coleman, *Nat. Nanotechnol.* **2008**, *3*, 563.
[18] a) X. Li, Y. Zhu, W. Cai, M. Borysiak, B. Han, D. Chen, R. D. Piner, L. Colombo, R. S. Ruoff, *Nano Lett.* **2009**, *9*, 4359; b) K. S. Kim, Y. Zhao, H. Jang, S. Y. Lee, J. M. Kim, K. S. Kim, J. H. Ahn, P. Kim, J. Y. Choi, B. H. Hong, *Nature* **2009**, *457*, 706.
[19] a) P. Kumar, *RSC Adv.* **2013**, *3*, 11987; b) U. Maitra, H. Matte, P. Kumar, C. N. R. Rao, *Chimia* **2012**, *66*, 941.
[20] P. Kumar, L. S. Panchakarla, C. N. R. Rao, *Nanoscale* **2011**, *3*, 2127.
[21] D. V. Kosynkin, A. L. Higginbotham, A. Sinitskii, J. R. Lomeda, A. Dimiev, B. K. Price, J. M. Tour, *Nature* **2009**, *458*, 872.
[22] M. M. Stylianakis, M. Sygletou, K. Savva, G. Kakavalakis, E. Kymakis, E. Stratakis, *Adv. Opt. Mater.* **2015**, DOI:10.1002/adom.201400450.
[23] E. Stratakis, K. Savva, D. Konios, C. Petridis, E. Kymakis, *Nanoscale* **2014**, *6*, 6925.
[24] Z. Yin, J. Zhu, Q. He, X. Cao, C. Tan, H. Chen, Q. Yan, H. Zhang, *Adv. Energy Mater.* **2014**, *4*, 1300574.
[25] G. Kakavelakis, D. Konios, E. Stratakis, E. Kymakis, *Chem. Mater.* **2014**, *26*, 5988.
[26] F. Bonaccorso, Z. Sun, T. Hasan, A. C. Ferrari, *Nat. Photon.* **2010**, *4*, 611.
[27] B. Bae, H. Kim, Y. Lee, X. F. Xu, J. S. Park, Y. Zheng, J. Balakrishnan, T. Lei, H. R. Kim, Y. I. Song, Y. J. Kim, K. S. Kim, B. Ozyilmaz, J. H. Ahn, B. H. Hong, S. Iijima, *Nat. Nanotechnol.* **2010**, *5*, 574.
[28] S. Park, J. An, J. R. Potts, A. Velamakanni, S. Murali, R. S. Ruoff, *Carbon* **2011**, *49*, 3019.
[29] a) P. Kumar, K. S. Subrahmanyam, C. N. R. Rao, *Int. J. Nanosci.* **2011**, *10*, 559; b) P. Kumar, B. Das, B. Chitara, K. S. Subrahmanyam, K. Gopalakrishnan, S. B. Krupanidhi, C. N. R. Rao, *Macromol. Chem. Phys.* **2012**, *213*, 1146; c) E. Kymakis, C. Petridis, T. D. Anthopoulos, E. Stratakis, *IEEE J. Sel. Top. Quantum Electron.* **2014**, *20*, 6573325
[30] F. Bonaccorso, A. Lombardo, T. Hasan, Z. Sun, L. Colombo, A. C. Ferrari, *Mater. Today* **2012**, *15*, 564.
[31] D. Konios, M. M. Stylianakis, E. Stratakis, E. Kymakis, *J. Colloid Interface Sci.* **2014**, *430*, 108.
[32] Y. Xu, G. Long, L. Huang, Y. Huang, X. Wan, Y. Ma, Y. Chen, *Carbon* **2010**, *48*, 3308.
[33] E. Kymakis, E. Stratakis, M. M. Stylianakis, E. Koudoumas, C. Fotakis, *Thin Solid Films* **2011**, *520*, 1238.
[34] Z. Yin, S. Sun, T. Salim, S. Wu, X. Huang, Q. He, Y. M. Lam, H. Zhang, *ACS Nano* **2010**, *4*, 5263.
[35] E. Kymakis, K. Savva, M. M. Stylianakis, C. Fotakis, E. Stratakis, *Adv. Funct. Mater.* **2013**, *23*, 2742.
[36] H. Wu, L. Hu, M. W. Rowell, D. Kong, J. J. Cha, J. R. McDonough, J. Zhu, Y. Yang, M. D. McGehee, Y. Cui, *Nano Lett.* **2010**, *10*, 4242.
[37] J. van de Groep, P. Spinelli, A. Polman, *Nano Lett.* **2012**, *12*, 3138.
[38] J. Zou, H. L. Yip, S. K. Hau, A. K. Y. Jen, *Appl. Phys. Lett.* **2010**, *96*, 203301.
[39] J. Bai, X. Zhong, S. Jiang, Y. Huang, X. Duan, *Nat. Nanotechnol.* **2010**, *5*, 190.
[40] N. E. Sosa, J. Liu, C. Chen, T. J. Marks, M. C. Hersam, *Adv. Mater.* **2009**, *21*, 721.
[41] L. Zhang, S. Diao, Y. Nie, K. Yan, N. Liu, B. Dai, Q. Xie, A. Reina, J. Kong, Z. Liu, *J. Am. Chem. Soc.* **2011**, *133*, 2706.
[42] Z. Zeng, X. Huang, Z. Yin, H. Li, Y. Chen, Q. Zhang, J. Ma, F. Boey, H. Zhang, *Adv. Mater.* **2012**, *24*, 4138.
[43] Z. L. Wang, D. Xu, H. G. Wang, Z. Wu, X. B. Zhang, *ACS Nano* **2013**, *7*, 2422.

© 2015 WILEY-VCH Verlag GmbH & Co. KGaA, Weinheim

[44] Y. Zhu, S. Murali, M. D. Stoller, K. J. Ganesh, W. Cai, P. J. Ferreira, A. Pirkle, R. M. Wallace, K. A. Cychosz, M. Thommes, D. Su, E. A. Stach, R. S. Ruoff, *Science* **2011**, *332*, 1537.
[45] Q. Zhang, X. Wan, F. Xing, L. Huang, G. Long, N. Yi, W. Ni, Z. Liu, J. Tian, Y. Chen, *Nano Res.* **2013**, *6*, 478.
[46] A. R. b. M.Yusoff, S. J. Lee, F. K. Shneider, W. J. da Silva, J. Jang, *Adv. Energy Mater.* **2014**, *4*, 1301989.
[47] P. Kumar, K. S. Subrahmanyam, C. N. R. Rao, *Mater. Exp.* **2011**, *1*, 252.
[48] M. F. El-Kady, R. B. Kaner, *Nat. Commun.* **2013**, *4*, 1475.
[49] H. Tian, H.-Y. Chen, T. -L.Ren, C. Li, Q.-T. Xue, M. A. Mohammad, C. Wu, Y. Yang, H.-S. P. Wong, *Nano Lett.* **2014**, *14*, 3214.
[50] A. Y. Vorobyev, C. Guo, *Laser Photon. Rev.* **2013**, *7*, 385.
[51] E. Stratakis, *Sci. Adv. Mater.* **2012**, *4*, 407.
[52] B. N. Chichkov, C. Momma, S. Nolte, F. Von Alvensleben, A. Tunnermann, *Appl. Phys. A* **1996**, *63*, 109.
[53] M. F. El-Kady, R. B. Kaner, *ACS Nano* **2014**, *8*, 8725.
[54] Y. L. Zhang, Q. D. Chen, H. Xia, H. B. Sun, *Nano Today* **2010**, *5*, 435.
[55] D. Li, M. B. Muller, S. Gilje, R. B. Kaner, G. G. Wallace, *Nat. Nanotechnol.* **2008**, *3*, 101.
[56] I. K. Moon, J. Lee, R. S. Ruoff, H. Lee, *Nat. Commun.* **2010**, *1*, 73.
[57] S. Das, P. Sudhagar, E. Ito, D.-Y. Lee, S. Nagarajan, S. Y. Lee, W. S. Kang, W. Choi, *J. Mater. Chem.* **2012**, *22*, 20490.
[58] S. Pang, H. N. Tsao, X. Feng, K. Mullen, *Adv. Mater.* **2009**, *21*, 3488.
[59] H. B. Jiang, Y. L. Zhang, D. D. Han, H. Xia, J. Feng, Q. D. Chen, Z. R. Hong, H. B. Sun, *Adv. Funct. Mater.* **2014**, *24*, 4595.
[60] S. M. Eaton, *Opt. Express* **2005**, *13*, 4708.
[61] R. Osellane, *J. Opt. Soc. Am. B* **2003**, *20*, 1559.
[62] Y. C. Li, T. F. Yeh, H. C. Huang, H. Y. Chang, C. Y. Lin, L. C. Cheng, C. Y. Chang, H. Teng, S. J. Chen, *Opt. Express* **2014**, *22*, 19726.
[63] J. B. Park, W. Xiong, Y. Gao, M. Qian, Z. Q. Xie, M. Mitchell, Y. S. Zhou, G. H. Han, L. Jiang, Y. F. Lu, *Appl. Phys. Lett.* **2011**, *98*, 123109.
[64] a) T. Kim, H. Kim, S. W. Kwon, Y. Kim, W. K. Park, D. H. Yoon, A.-R. Jang, H. S. Shin, K. S. Suh, W. S. Yang, *Nano Lett.* **2012**, *12*, 743; b) J. W. Bai, X. Zhong, S. Jiang, Y. Huang, X. F. Duan, *Nat. Nanotechnol.* **2010**, *5*, 190.
[65] J. S. Oh, S. H. Kim, T. Hwang, H.-Y. Kwon, T. H. Lee, A. H. Bae, H. R. Choi, J. D. Nam, *J. Phys. Chem. C* **2013**, *113*, 663.
[66] Y.-Q. Bie, Y.-B. Zhou, Z.-M. Liao, K. Yan, S. Liu, Q. Zhao, S. Kumar, H.-C. Wu, G. S. Duesberg, G. L. W. Cross, J. Xu, H. Peng, Z. Liu, D.-P. Yu, *Adv. Mater.* **2011**, *23*, 3938.
[67] Q. He, H. G. Sudibya, Z. Yin, S. Wu, H. Li, F. Boey, W. Huang, P. Chen, H. Zhang, *ACS Nano* **2010**, *4*, 3201.
[68] M. N. Saleh, G. Lubineaou, *Solar Energy Mater. Solar Cells* **2015**, *139*, 199.
[69] J. B. Wu, H. A. Becerril, Z. N. Bao, Z. F. Liu, Y. S. Chen, P. Peumans, *Appl. Phys. Lett.* **2008**, *92*, 263302.
[70] V. C. Tung, L. M. Chen, M. J. Allen, J. K. Wassei, K. Nelson, R. B. Kaner, Y. Yang, *Nano Lett.* **2009**, *9*, 1949.
[71] J. Geng, L. Liu, S. B. Yang, S. C. Youn, D. W. Kim, J. S. Lee, J. K. Choi, H. T. Jung, *J. Phys. Chem. C* **2010**, *114*, 14433.
[72] J. H. Huang, J. H. Fang, C. C. Liu, C. W. Chu, *ACS Nano* **2011**, *5*, 6262.
[73] Z. He, C. Zhong, X. Huang, W. Y. Wong, H. Wu, L. Chen, S. Su, Y. Cao, *Adv. Mater.* **2011**, *23*, 4636.
[74] G. Kakavelakis, E. Stratakis, E. Kymakis, *Chem. Commun.* **2014**, *50*, 5285.

© 2015 WILEY-VCH Verlag GmbH & Co. KGaA, Weinheim